MATERIALS CHEMISTRY FRONTIERS

RESEARCH ARTICLE

View Article Online
View Journal

Cite this: DOI: 10.1039/d5qm00681c

A Pd-functionalized β-ketoenamine COF for efficient hydrogen sensing under ambient conditions

Sujith Benarzee Nallamalla,[a] Raja Karreddula,[b] Balaji Rao Ravuri[c] and Surendra Babu Manabolu Surya *[a]

Hydrogen sensing materials are vital for energy and environmental safety, as hydrogen's high energy density and flammability demand rapid and reliable detection at low concentrations under ambient conditions. Here, we report a palladium nanoparticle-functionalized β-ketoenamine-linked covalent organic framework (Pd@TAPT-COF) that enables efficient room-temperature hydrogen sensing. Structural analyses (solid-state ^{13}C CP-MAS NMR, FTIR, and XPS) confirm successful Pd incorporation into the TAPT-COF, with characteristic shifts in C=O and C=N peaks evidencing strong Pd–TAPT COF interactions. The ^{13}C NMR spectra show a shift in the C=O peak signal from 182 ppm to 190 ppm and the appearance of a new peak at 22 ppm, confirming Pd interactions with keto carbons. FTIR showed a C=O stretching shift from 1622 cm^{-1} to 1613 cm^{-1} and a C=N shift from 1497 to 1499 cm^{-1} after Pd doping. XPS O1s spectra exhibited distinct peaks at ~530.8 eV (C=O) and ~532.5 eV (Pd–O), providing further evidence of Pd coordination with oxygen-containing groups. The Pd@TAPT-COF exhibited exceptional chemiresistive performance toward H_2, attaining a response (R_a/R_g) of 10, with a fast response time (T_{res}) of 4 s and a recovery time (T_{rec}) of 3 s at 1 ppm, along with superior selectivity and stability. Density functional theory (DFT) calculations support these results, revealing strong H_2 binding energies (−484.57 kJ mol^{-1}), a narrowed HOMO–LUMO gap (~2.82 eV), increased orbital hybridization near the Fermi level, and efficient charge transfer from Pd–H interactions. These results indicate that the integration of Pd catalytic sites within the pristine TAPT-COF facilitates rapid, selective, and reversible H_2 detection, making the Pd@TAPT-COF a strong sensing material for future energy and safety sensor applications.

Received 16th September 2025,
Accepted 1st December 2025

DOI: 10.1039/d5qm00681c

rsc.li/frontiers-materials

1. Introduction

Hydrogen (H_2) is a pivotal energy carrier in the global transition toward sustainable energy and low-emission energy system options.[1] With the world energy sector transitioning to low-carbon fuel, hydrogen (H_2) has arrived not just as a fuel but as a de-carbonization tool in aviation and long-distance transport hard-to-abate sectors.[2,3] Its gravimetric energy density of 120 MJ kg^{-1} combined with its use in fuel cells with no combustion emissions makes it one of the few feasible ways of achieving net-zero emissions. Yet, the same promise is accompanied by a paradox: the more hydrogen that is stored, transported, and combusted, the greater the risk of undetectable, explosive, and environmentally harmful leaks.[4] Hydrogen's atmospheric lifetime is approximately two years, and it ranks as the second most abundant reactive gas in the troposphere after methane. Hydrogen leakage not only poses safety risks but also affects atmospheric chemistry, with potential climate impacts.[5,6] While not a direct greenhouse gas, H_2 indirectly contributes to climate change by extending methane's lifetime through hydroxy radical ($OH^{\bullet}$) depletion and increasing stratospheric water vapour levels, which impact radiative forcing. With the rising acceptance of hydrogen worldwide with more than 200 large-scale projects in the pipelines in recent years, sensor technologies fall behind in preparation, particularly for ambient, trace-level detection.[7] This necessitates the development of highly sensitive and selective hydrogen sensors capable of detecting leaks early and preventing accidents.[7] Despite advancements in developed hydrogen

[a] Department of Chemistry, School of Science, GITAM deemed to be University, Hyderabad campus, Hyderabad-502329, Telangana, India.
E-mail: snallama2@gitam.in, smanabol@gitam.edu
[b] Department of Chemistry, Rajeev Gandhi Memorial College of Engineering and Technology (Autonomous), Nandyal, Andhra Pradesh-518501, India.
E-mail: rajachem786@gmail.com
[c] Department of Physics and Astronomical Sciences, Central University of Jammu, Rahya-Suchani, Samba, Jammu & Kashmir 18114, India.
E-mail: balaji.nsm@cujammu.ac.in

sensing technologies, including metal–oxide semiconductor sensors, palladium-based resistive sensors, electrochemical sensors, and optical sensors, significant challenges remain in achieving highly efficient, selective, and low-power consumption sensors for real-world applications.[8–10] While conventional metal–oxide sensors demand high temperatures and excessive energy consumption, and exhibit limited long-term stability, electrochemical sensors, although sensitive, exhibit performance degradation under humid conditions, making them less reliable for industrial and environmental monitoring.[11,12] Moreover, most commercially available sensors suffer from poor selectivity, leading to interference from other reducing gases. Additionally, many conventional sensors lack selectivity, as they are susceptible to interference from gases such as methane, ammonia, and volatile organic compounds (VOCs). These limitations highlight the need for hydrogen sensors that operate efficiently at room temperature (RT) with high sensitivity, selectivity, and long-term stability. This problem has rekindled interest in molecularly engineered sensing materials, specifically in covalent organic frameworks (COFs).[13–15] These are 2D or 3D polymeric crystals formed from organic linkers *via* dynamic covalent chemistry. Their modular structure, π-conjugation, and porous nature enable researchers to control gas accessibility and electronic response.[16–18] COFs are, however, poor conductors and do not contain active sites to catalyze processes such as H_2 dissociation, a requirement for efficient chemiresistive sensing.[19–21] Herein, palladium nanoparticles (Pd NPs) are incorporated into the backbone of a β-ketoenamine-linked COF, combining catalytic function and framework transport into a single sensing material.[22,23] Pd is famously known for its spillover mechanism, breaking down H_2 into atomic hydrogen (H) that diffuses through surfaces and forming PdH_x species, which change electronic properties quantifiable through resistance changes.[24] Incorporating Pd into the COF not only activates the material toward hydrogen but also amplifies the signal through charge delocalisation in the conjugated framework. In the case of the Pd@TAPT-COF, this synergy is especially strong.[25] Recently, Chu *et al.* demonstrated an atomically dispersed Pd sub-metallene on a 2D Mo_2TiC_2 MXene that achieved ultrafast hydrogen response (4.8 s) and recovery (1.6 s) at room temperature due to synergistic Pd–Pd interactions, facilitating rapid H_2 dissociation.[26] This highlights the importance of atomic-level Pd coordination in accelerating hydrogen activation, a principle also underlying the design of the present work. The TAPT (1,3,5-tris-(4-aminophenyl)triazine) core provides high nitrogen coordination and a stable backbone, whereas β-ketoenamine linkages provide chemical stability and π-conduction. Pd coordination at keto and imine sites, established through ^{13}C NMR, FTIR, and XPS, leads to a material with an engineered electronic landscape and high surface accessibility.[27–29] The sensor reacts to 1 ppm of H_2 within a mere 4 seconds and recovers in 3 seconds, performing better than the majority of known Pd-based sensors (Table 1), due to synergistic interactions between Pd and COFs, which enhance charge transport, reduce sensor drift, and improve selectivity by minimizing cross-sensitivity to interfering gases.[30,31] The DFT-based calculations reveal striking changes in binding energies (from −69.96 kJ mol^{-1} for the pristine COF to −484.57 kJ mol^{-1} after Pd functionalization), band-gap narrowing (from 3.56 eV to 2.82 eV), and a higher density of states at the Fermi level, indicating real electronic hybridization. These results not only demonstrate the sensor's performance but also provide a rationally designed framework for application in next-generation molecular sensors, where active site tuning, orbital engineering, and framework adjustment can be systematically controlled by computational methods.

In this work, we present a Pd@TAPT-COF that uniquely combines a chemically stable β-ketoenamine linkage with a nitrogen-rich TAPT core, providing a robust framework supporting highly dispersed Pd nanoparticles. This framework enables ultrafast and sensitive hydrogen sensing at ambient temperature, outperforming most previously reported Pd-functionalized COFs. Complementary experimental characterizations coupled with DFT calculations provide detailed mechanistic insights into the catalytic and electronic interactions, developing the Pd@TAPT-COF as an advanced material that advances Pd-based hydrogen sensor technology.

2. Results and discussion

2.1. Synthesis and morphological analysis

This study involved the synthesis of a covalent organic framework (COF) using a Schiff base condensation reaction between

Table 1 Summary of the literature on COF-based chemiresistive H_2 gas sensors

S. no.	COF material	Response time (t_{res})	Recovery time (t_{rec})	T (°C)	Target gas	Conc. (%)	Ref.
1	Pd nanopattern	1.5 s	12 s	RT	H_2	1	52
2	eNT COF	5.15 s	3.9 s	200	H_2	1	55
3	$Pd_{0.5}PT_{0.5}$ bimetallic NPs	7.5 s	92 s	RT	H_2	1	56
4	Pd/Pt nanopattern	2 s	20 s	40	H_2	1	57
5	Pd@WS_2 nanosheets	119 s	370 s	7.8	H_2	5	58
6	Pt/g-C_3N_4	39 s	5 s	RT	H_2	1	59
7	Pd@MoS_2 nanosheets	40 s	83 s	100	H_2	5	28
8	Pd@CVD-graphene	2.1 s	463 s	4.1	H_2	0.05	60
9	PdII@CrPy	13.2 s	10.3 s	RT	H_2	1	16
10	Pd@graphene nanoribbon	60 s	90 s	25	H_2	0.1	61
11	Pd@amicPT	5.3 s	3.5 s	30	H_2	1	42
12	Pd@TAPT-COF	4 s	3 s	RT	H_2	0.0001	This work

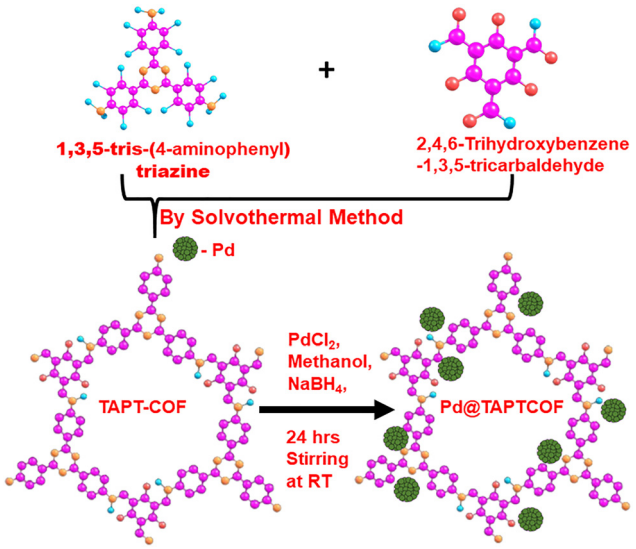

Fig. 1 Schematic representation of the synthesis of the TAPT-COF and Pd@TAPT-COF.

aldehyde- and amine-based linkers under solvothermal conditions with slight modifications.[32] Specifically, the TAPT-COF was synthesized using 2,4,6-trihydroxybenzene-1,3,5-tricarbaldehyde and 1,3,5-tris-(4-aminophenyl) triazine, an amine-based linker. To enhance its H_2 sensing properties under ambient conditions, palladium nanoparticles (Pd NPs) were incorporated into the TAPT-COF *via* post-synthetic modification,[33] and the detailed synthesis procedures are provided in Fig. 1 and Section S1 (SI).

To confirm the successful incorporation of Pd into the TAPT-COF and its impact on the structural and electronic properties, we have performed ^{13}C CP-MAS solid-state NMR (Fig. 2a (pristine TAPT-COF) and Fig. 2b (Pd@TAPT-COF)), which revealed a significant structural modification upon Pd functionalization. In the pristine TAPT-COF, characteristic peaks were observed at 182 ppm (C═O), 168–146 ppm (aromatic C═N/C═C), 129 ppm (sp^2 carbons), and 60 ppm (C–O or C–N functional groups). Upon Pd incorporation, notable spectral shifts occurred, including the C═O peak shift from 182 ppm to 190 ppm and the aromatic carbon shift to 150–138 ppm, indicating electronic perturbations.[34] Additionally, the appearance of a new peak at 22 ppm (potential aliphatic species from Pd coordination in the TAPT-COF) and the absence of the 60 ppm peak suggested Pd interactions with oxygen- or nitrogen-containing sites in the TAPT-COF structure. These spectral shifts confirmed the successful Pd incorporation, likely through forming keto (C═O) and imine (C═N) groups, thereby modifying the electronic environment of the TAPT-COF while maintaining its overall structural integrity.[35] Fourier transform infrared (FTIR) spectral analysis was employed to elucidate the structural characteristics and the impact of Pd incorporation on the functional groups of the pristine TAPT-COF and Pd@TAPT-COF (Fig. 2c). The spectrum of the pristine TAPT-COF exhibited a prominent peak at 1622 cm^{-1}, attributable to the stretching vibration of the keto (C═O) group, and this indicates that the enamine bond formation in the aldehyde monomer transforms the (═C–OH) group into a (═C═O) group. The peak at 1497 cm^{-1} corresponds to the (C═N) stretching within the imine linkages, thus confirming the successful formation of the TAPT-COF. Additionally, the C═C stretching peak at 1575 cm^{-1} indicated the presence of a conjugated π–π system inherent to the COF[36]. Following Pd doping, noticeable shifts in these vibrational bands were observed, with the C═O peak shifting to 1613 cm^{-1} and the C═N peak shifting to 1499 cm^{-1}.[37] These peak shifts suggested electronic interactions between Pd and the imine groups of the TAPT-COF. The observed spectral shifts confirmed Pd-induced electronic modifications, which make the TAPT-COF stable and efficient for H_2 sensing at room temperature. To further support these findings, PXRD analysis confirmed the crystallinity and structural integrity of the COFs (Fig. 2d). PXRD analysis was performed to evaluate the crystallinity and structural changes upon palladium incorporation into the TAPT-COF. The pristine TAPT-COF exhibited reflections at ∼5.73°, ∼9.89°, ∼18.70°, and ∼26.41°, corresponding to the (100), (110), (210), and (001) planes, with calculated *d*-spacings of 15.42 Å, 8.94 Å, 4.74 Å, and 3.37 Å, respectively (Table S1, SI), while a broader diffraction peak at ∼26.4° was assigned to the (001) plane, indicating π–π stacking between adjacent 2D layers of COFs.[32,38,39] These peaks confirm the formation of a highly ordered 2D framework with eclipsed AA stacking.[40] Upon incorporation of the Pd@TAPT-COF (Fig. 2d), the TAPT-COF related peaks remained but showed reduced intensity and slight shifts (the (110) peak shifted to 10.08°, d = 8.77 Å), indicating lattice distortion due to Pd incorporation. Additionally, new peaks appeared at ∼30.66°, ∼40.02°, ∼46.76°, ∼50.84°, and ∼68.11°, with the corresponding *d*-spacings of 2.91 Å, 2.25 Å, 1.94 Å, 1.74 Å, and 1.37 Å. These match the (111), (200), (220), (311), and (222) planes of face-centered cubic (FCC) Pd consistent with JCPDS No. 46-1043.[41] The presence of these Pd-specific reflections indicates successful formation of crystalline Pd NPs within the TAPT-COF, enhancing its functional potential for H_2 sensing. The XPS survey spectrum of the TAPT-COF and Pd@TAPT-COF confirmed the presence of C, N, O, and Pd, aligning well with the above results (^{13}C CP-MAS NMR and FTIR analyses).[42] The details of the C1s and N1s spectra of both the pristine TAPT-COF and Pd@TAPT-COF are shown in Fig. S1a, b and S2a, b. The deconvoluted spectra of O1s with two different binding energy peaks of the TAPT-COF at ∼535 eV (C–O interaction) and ∼531 eV (C═O) (Fig. 2e) confirmed that the TAPT-COF is primarily in the enol form. Quantitative analysis (Table S2, SI) revealed that the TAPT-COF exhibits a C═O peak area percentage of 65.1% and a C–O percentage of 34.8%, giving a C═O/C–O ratio of 1.87. Similarly, the O1s spectra of the Pd@TAPT-COF (Fig. 2f) exhibited distinct peaks corresponding to C═O at ∼530.8 eV and Pd–O interaction at ∼532.5 eV.[33] Notably, the C═O contribution increased to 79.6% with a corresponding decrease in C–O to 20.4%, resulting in a significantly higher C═O/C–O ratio of 3.90 (Table S2, SI). The shifts in binding energy compared to the pristine TAPT-COF suggest strong interactions between Pd and the –C═O– form of

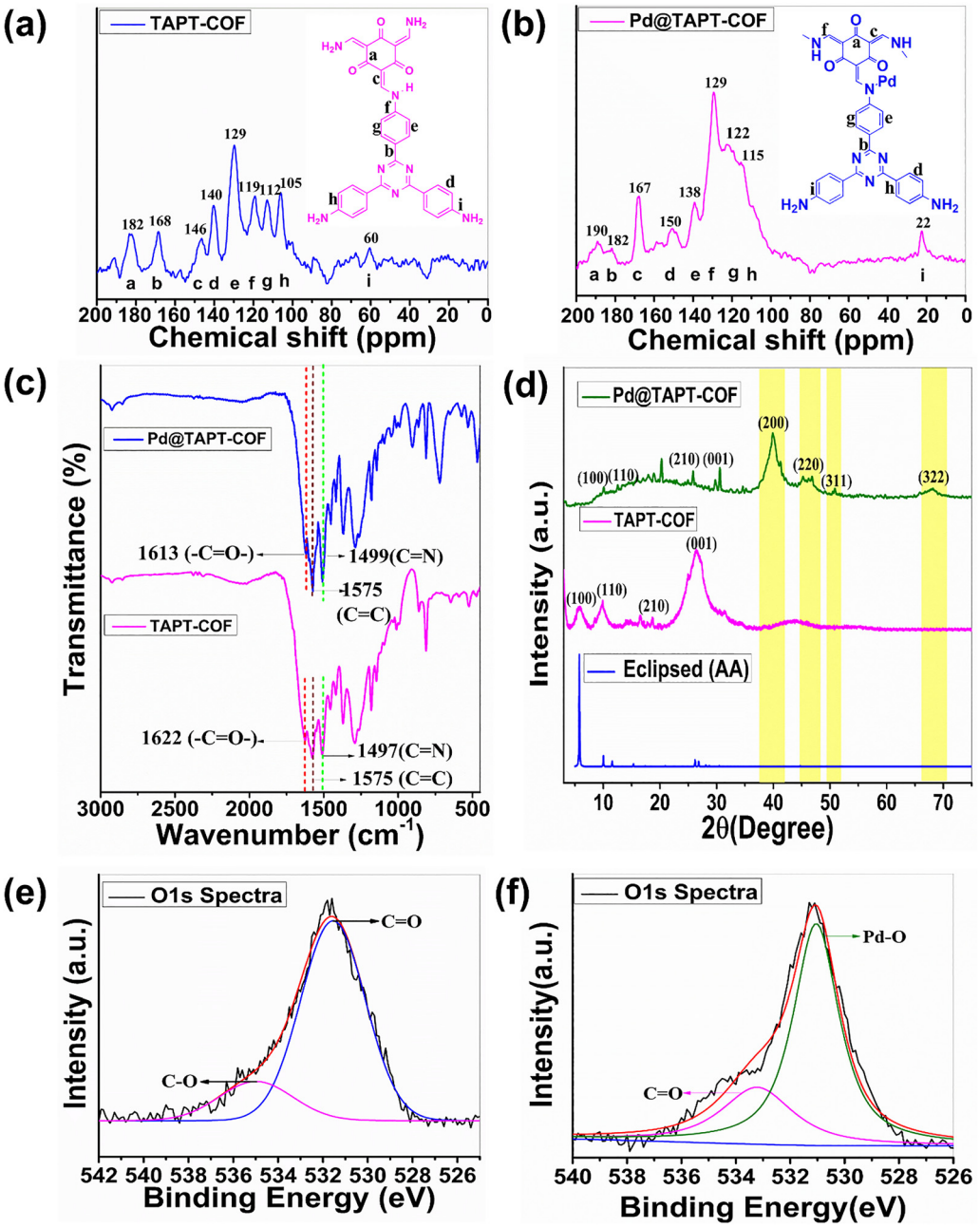

Fig. 2 (a) Solid-state ^{13}C CP-MAS NMR spectra of the TAPT-COF. (b) Solid-state ^{13}C CP-MAS NMR spectra of the Pd@TAPT-COF, confirming framework formation and Pd incorporation; (c) FT-IR spectra showing characteristic vibrations of C═N, C═O, and C═C in the TAPT-COF and their shifts in the Pd@TAPT-COF, indicating Pd incorporation; (d) PXRD patterns of the TAPT-COF and Pd@TAPT-COF showing retained crystallinity with indexed peaks; (e) and (f) O 1s XPS spectra showing C–O and C═O in the TAPT-COF, with an additional Pd–O peak in the Pd@TAPT-COF, confirming successful incorporation of Pd.

the TAPT-COF. Additionally, the Pd@TAPT-COF (Fig. S2c, SI) showed two distinct peaks at ~335.6 eV and ~340.8 eV, corresponding to Pd $3d_{5/2}$ and $3d_{3/2}$, respectively, indicating Pd coordination with oxygen and nitrogen sites. These results collectively indicated successful Pd integration into the TAPT-COF.[43]

The synthesised pristine TAPT-COF and Pd@TAPT-COF exhibited exceptional surface morphologies that play a crucial role in their H_2 sensing performance. The FESEM images of the pristine TAPT-COF (Fig. 3a–c) showed a highly porous and fibrous network-like morphology, characteristic of the well-ordered TAPT-COF structure. After Pd doping in the TAPT-COF, significant morphological changes were observed in the FESEM image of the Pd@TAPT-COF (Fig. 3e–g), which exhibited a granular morphology with the fibrous network partially masked by Pd nanoparticles. The HR-TEM images show uniformly dispersed dark contrast regions corresponding to Pd nanoparticles embedded within the TAPT-COF. In addition,

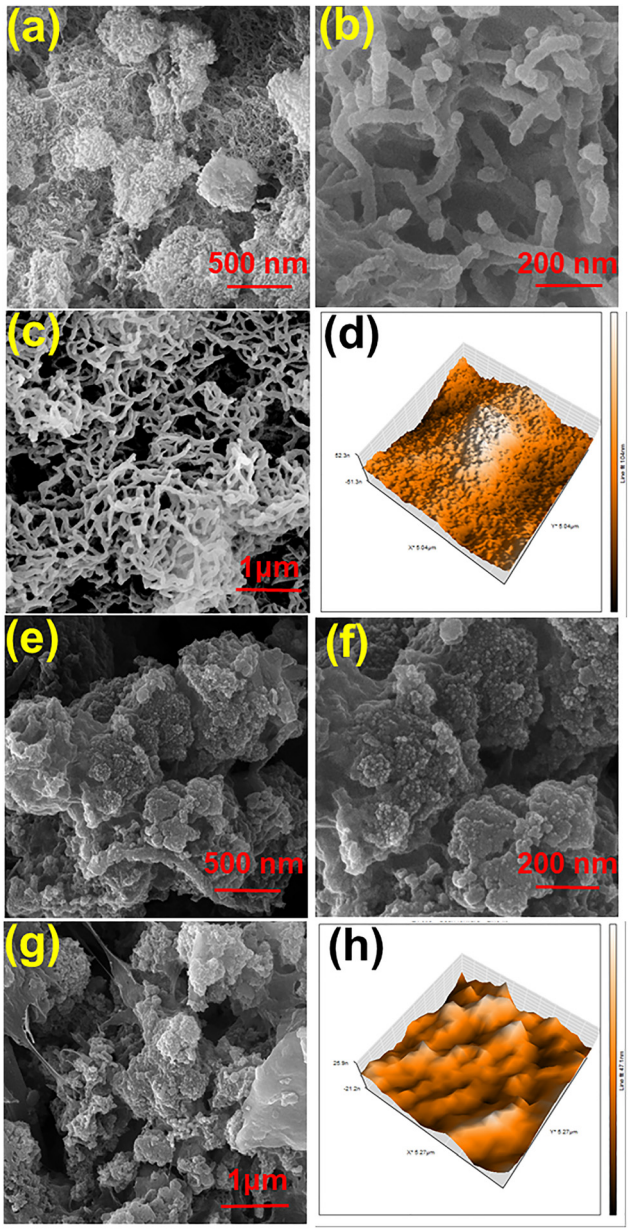

Fig. 3 (a)–(c) FESEM images of the TAPT-COF at different magnifications showing a fibrous and porous network morphology; (d) AFM image of the TAPT-COF indicating uniform surface roughness; (e)–(g) FESEM images of the Pd@TAPT-COF revealing aggregated and granular morphology due to Pd incorporation; and (h) AFM image of the Pd@TAPT-COF showing increased surface roughness after Pd loading.

elemental mapping (Fig. 4a–f and Fig. S3, SI) confirms a homogenous Pd distribution throughout the framework, indicating that the nanoparticles are primarily incorporated within the internal pore channels rather than only on the external surface. The slight decrease in BET surface area and pore volume after Pd loading further supports partial occupancy of the intrinsic pore network by Pd. This morphological change suggests that Pd NPs have been successfully doped into the TAPT-COF, potentially through coordination interactions with the keto group in the TAPT-COF structure. The low-magnification images (Fig. 4a–c) illustrate a network-like structure with particle sizes ranging from ~500 nm to 50 nm, indicative of hierarchical porosity. The high-resolution TEM (HRTEM) image (Fig. 4d) further confirmed its crystallinity, displaying lattice spacings of 0.62 nm and 2.69 nm, corresponding to the (001) and (100) planes, respectively.[44] The SAED pattern (Fig. 4e) provides additional evidence of its polycrystalline nature, characterised by distinct diffraction rings that reflect good ordering within the framework. The HAADF-STEM image (Fig. 4f) exhibited uniform contrast, reflecting the elemental homogeneity of the TAPT-COF, consistent with its composition. Following Pd incorporation, Fig. 4g and h shows the TEM images of the Pd@TAPT-COF, which exhibited a denser morphology with dark contrast regions indicating that Pd NPs were uniformly distributed within the TAPT-COF matrix. The TEM-derived pore size distribution (Fig. 4i) shows a dominant mesopore size of ~7 nm with a narrow distribution, along with a few larger pores, confirming hierarchical porosity. Such a porous network, combined with well-dispersed Pd NPs, can enhance gas diffusion and increase active site accessibility. The high-resolution TEM image (Fig. 4j) provided further structural validation, showing well-defined lattice fringes with spacings of 0.89 nm, 2.32 nm, and 2.89 nm, corresponding to the (110), (210), and (111) planes, respectively.[27]

The SAED pattern (Fig. 4k) further supported the polycrystalline nature of the Pd@TAPT-COF, as evidenced by sharp diffraction rings characteristic of metallic Pd. The HAADF-STEM image (Fig. 4l) distinctly highlights atomic-scale contrast, where the bright regions correspond to Pd NPs, confirming their homogenous dispersion within the TAPT-COF matrix through Z-contrasting. Elemental mapping (Fig. S3a–d, SI) demonstrates a homogeneous distribution of carbon, nitrogen, oxygen, and palladium throughout the TAPT-COF, confirming uniform incorporation of Pd. The high resolution Pd mapping in Fig. S3 provides clearer contrast, indicating that Pd nanoparticles are present within the internal pore channels rather than only on the external surface. Such uniform Pd dispersion within the porous COF facilitates efficient H_2 diffusion and increases the number of active sites, thereby enhancing H_2 sensing performance. The surface morphology of the TAPT-COF and Pd@TAPT-COF samples, examined through atomic force microscopy (AFM) at magnifications of 10 $\mu m^2 \times 10\ \mu m^2$, is illustrated in Fig. 3d and Table S3 (SI). The AFM contact mode was used to measure the area roughness parameters of the TAPT-COF, yielding a mean surface roughness (Sa) of 14.39 nm for the TAPT-COF and 16.23 nm for the Pd@TAPT-COF, respectively. This increase in surface roughness after Pd incorporation confirms successful doping, likely due to the deposition of Pd nanoparticles on the TAPT-COF, which in turn may influence the porosity characteristics. To further understand the impact of Pd incorporation on the porous structure, nitrogen adsorption–desorption studies (Fig. S4a–d and Table S4, SI) were carried out. Both the TAPT-COF and Pd@TAPT-COF showed type IV isotherms with H3-type hysteresis loops, which are typical of mesoporous materials with slit-shaped pores. The

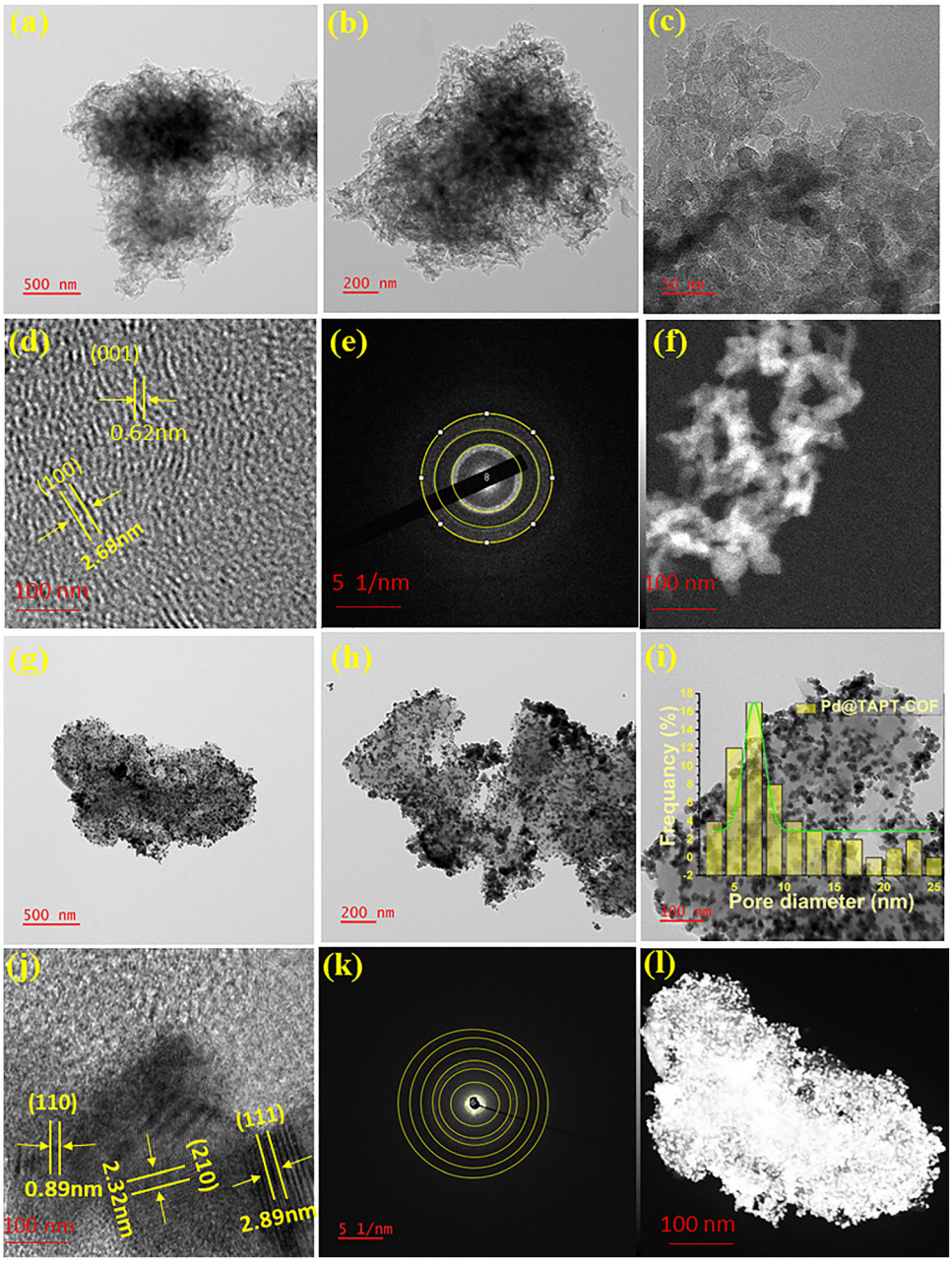

Fig. 4 (a)–(c) TEM images of the TAPT-COF, depicting the overall particle distribution and structure; (d) HRTEM image of the TAPT-COF, highlighting lattice fringes; (e) SAED pattern of the TAPT-COF, exhibiting crystallinity; (f) HAADF image of the TAPT-COF confirming homogenous contrast; (g) and (h) TEM images of the Pd@TAPT-COF showing the dispersion of Pd NPs on the COF surface; (i) TEM image of the Pd@TAPT-COF integrated with the TEM-derived pore size distribution histogram, confirming a uniform mesoporous structure (~7 nm) and well-dispersed Pd NPs on the TAPT-COF surface; (j) HRTEM image of the Pd@TAPT-COF revealing lattice fringes corresponding to Pd (110), (111), and (210) planes, confirming Pd NP incorporation; (k) SAED pattern of the TAPT-COF, exhibiting sharp diffraction rings, indicating improved crystallinity; and (l) HAADF image of the Pd@TAPT-COF showing dense Pd distribution.

TAPT-COF showed a higher nitrogen uptake (~200 $m^2 g^{-1}$ at $P/P_0 = 1.0$) and a larger average pore diameter of 45.7 nm, with a total pore volume of 0.271 $cm^3 g^{-1}$, whereas the Pd@TAPT-COF exhibited a slightly lower surface area (~150 $m^2 g^{-1}$), an average pore size of 42.1 nm, and a pore volume of 0.229 $cm^3 g^{-1}$, likely due to partial pore filling by Pd NPs. Despite this reduction, the preserved hysteresis loops and mesoporosity confirm that the intrinsic porous network of the TAPT-COF remains largely intact after Pd functionalization.[45] Although Pd incorporation causes a moderate reduction in surface area and pore size due to partial pore filling by Pd NPs, the preserved mesoporosity ensures sufficient gas diffusion; however, this reduction may limit adsorption capacity and sensitivity at very low hydrogen concentrations. To further elucidate the pore characteristics, *t*-plot and NLDFT analyses were performed (Fig. S5a and b, SI). The *t*-plot revealed a positive intercept, confirming the presence of micropores in both the TAPT-COF and Pd@TAPT-COF, with corresponding micropore volumes of 0.031 $cm^3 g^{-1}$ and

0.024 $cm^3\ g^{-1}$, respectively. The NLDFT pore size distribution (Fig. S5c and d, SI) exhibited a dominant peak below ~2 nm, along with a broader peak around ~3–4 nm, indicating a combined micro–mesoporous structure. After Pd incorporation, a slight reduction in pore size and volume was observed, suggesting partial filling of micropores by Pd NPs, while the preserved mesoporosity ensures adequate diffusion pathways for gas sensing. UV-Vis DRS (Fig. S5 and S6) revealed that the Pd@TAPT-COF shows higher absorbance, a red shift in the main transition (380 nm to 393 nm), and an extended absorption edge (348 to 440 nm), leading to a reduced band gap (3.56 eV to 2.82 eV) compared to the TAPT-COF. Following the characterisation of surface and porosity, thermogravimetric analysis (TGA) was performed to evaluate the thermal stability of both frameworks (Fig. S7, SI). The TAPT-COF exhibited an initial weight loss starting at 150 °C, with major decomposition occurring between 400 and 650 °C, leading to nearly complete mass loss at 700 °C.[46] In contrast, the Pd@TAPT-COF showed a more gradual decomposition profile with a residual mass of ~30% remaining at 800 °C. This improved thermal resistance, along with the presence of residual Pd content, confirms successful metal incorporation and indicates enhanced structural stability of the COF upon Pd doping.

2.2. Hydrogen sensing performance of the pristine TAPT-COF and Pd@TAPT-COF at ambient temperature

Hydrogen gas sensors are essential for ensuring safety in industrial and domestic environments due to the flammable nature of H_2 and its wide use as a clean energy carrier.[47] However, room temperature H_2 sensing remains a significant challenge owing to the low kinetic energy and reduced molecular reactivity of H_2 under ambient conditions. Most existing sensors require highly elevated operating temperatures, sufficient sensitivity, and rapid response, which limit their practicality for real-world and low-power consumption applications.[48] Therefore, the development of materials capable of detecting H_2 efficiently at room temperature with quick response and recovery is critical for enabling portable, energy-efficient, and real-time sensing technologies.[49,50] In this context, we tested the H_2 sensing behaviour of the TAPT-COF and its Pd-incorporated derivative (Pd@TAPT-COF) under ambient conditions, which showed fast response (4 s) and recovery times (3 s). These sensors exhibited distinct structural features of COFs, including keto groups, surface area, and porosity, which enhanced gas sensing by influencing the electronic properties and adsorption behaviour. This study evaluated the chemiresistive response of these COFs to H_2 at various concentrations of 1, 5, 10, 25, and 50 ppm (Fig. S8, SI). The H_2 sensing characteristics of these materials were further assessed by monitoring the changes in electrical resistance upon exposure to different H_2 concentrations at room temperature. The sensing response is represented by the ratio R_a/R_g, where R_a is the sensor resistance in air and R_g is the resistance under an H_2 gas environment. This ratio provides a measure of sensitivity, with higher values indicating a stronger sensor response. The response and recovery times are defined as the times required to reach 90% of the maximum resistance change upon exposure and 10% to the baseline after gas removal, respectively[51] (Fig. S9, SI). Additionally, current measurements under an applied voltage were used to monitor dynamic behaviour, with the saturation current indicating the steady-state value upon full hydrogen adsorption. A detailed explanation of these measurements and calculation methods is provided in Sections S2 and S3, SI.

The H_2 gas-sensing responses at 1, 5, 10, 25, and 50 ppm at ambient temperature for the chemiresistive pristine TAPT-COF material and Pd@TAPT-COF were found to be 1.14, 1.21, 1.34, 1.68, and 5.83 and 1.4, 1.6, 1.4, 1.7, and 10, respectively. Interestingly, it is observed from this study that the Pd@TAPT-COF showed an H_2 sensing response of 10 at 50 ppm, which is better than that of the pristine TAPT-COF. The TAPT-COF and Pd@TAPT-COF sensors' dynamic response and recovery characteristics are depicted in Fig. 5a and b for H_2 concentrations of 1, 5, 10, 25, and 50 ppm. The Pd@TAPT-COF sensor exhibited superior H_2 sensing response compared to the TAPT-COF at ambient temperature. Upon comparison of COFs' thin films at varying hydrogen concentrations, the sensor exhibited a detection limit of 1 ppm for H_2. The TAPT-COF sensor exhibited responses of 1.14, 1.21, 1.34, 1.68, and 5.83 to various H_2 concentrations, with the corresponding response times of 6 s, 8 s, 22 s, 20 s, and 18 s, respectively. The recovery times were 4 s, 12 s, 21 s, 22 s, and 17 s, respectively, as illustrated in Fig. 5a and Table S5 (SI). Similarly, the Pd-incorporated COF (Pd@TAPT-COF) sensor's response was found to be 1.4, 2.2, 3.2, 5.3, and 10 at various H_2 concentrations. The response times of the Pd@TAPT-COF were 4 s, 5 s, 10 s, 11 s, and 16 s, and the recovery times were found to be 3 s, 6 s, 12 s, 14 s, and 18 s (Fig. 5b and Table S8, SI). The response and recovery times of the COFs at 1 ppm – pristine TAPT-COF (t_{res} = 6 s, t_{rec} = 4 s at 1 ppm) and Pd@TAPT-COF (t_{res} = 4 s, t_{rec} = 3 s at 1 ppm) – indicated that the Pd@TAPT-COF shows superior sensing results compared to the TAPT-COF (Fig. 5c and d). The average recovery percentage of the TAPT-COF was 99.56%, and that of the Pd@TAPT-COF was 99.70% (Tables S5 and S6, SI). The enhanced recovery percentage of the Pd@TAPT-COF might be attributed to the catalytic and electronic properties of palladium. Based on the available literature on Pd-based H_2 sensors (Table 1), we observed that our material, Pd@TAPT-COF, showed exceptional sensitivity and a fast recovery time at room temperature at low concentrations of H_2 gas. In previously reported literature, Pd-decorated nanoribbons exhibited a relatively slow response and recovery (60 s and 90 s) even at a low concentration of 0.1% H_2[52] (Table 1), while Pd@MoS_2 nanosheets showed a response time of 40 s and a recovery time of 83 s at a higher concentration of 5% H_2 and an operating temperature of 100 °C.[28] In contrast, our COF material, Pd@TAPT-COF, showed a significantly faster response of 4 s and a recovery time of 3 s at an ultra-low hydrogen concentration of 0.0001% under ambient conditions. This superior performance is attributed to the high surface area, efficient conjugated framework, and well-dispersed Pd NPs in the TAPT-COF, which collectively facilitate rapid H_2 adsorption,

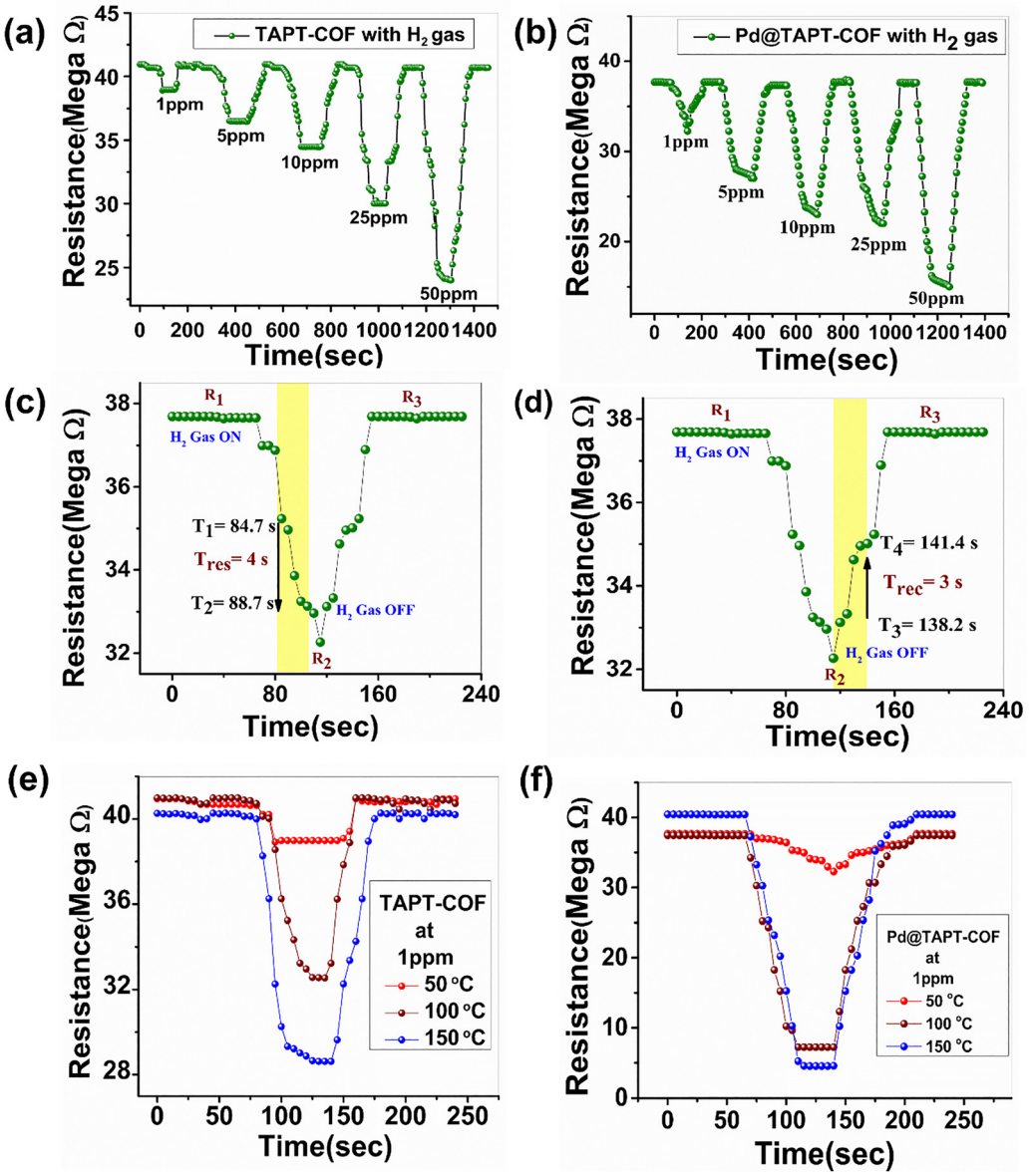

Fig. 5 Resistance curves of the (a) TAPT-COF and (b) Pd@TAPT-COF with H_2 gas sensing at concentrations of 1, 5, 10, 25, and 50 ppm at room temperature. (c) and (d) Enlarged resistance profiles of the Pd@TAPT-COF at 1 ppm H_2 showing the measured response and recovery times. Resistance *vs.* time curves of the (e) TAPT-COF and (f) Pd@TAPT-COF at 1 ppm H_2 at different temperatures (50 °C, 100 °C, and 150 °C) showing enhanced response at higher temperatures.

dissociation, and charge transport. A comprehensive performance comparison with other Pd-based hydrogen sensors is presented in Table 1.

Also, the enhanced sensing performance of the Pd@TAPT-COF compared to the pristine TAPT-COF can be attributed to the catalytic properties of palladium, which play a crucial role in improving hydrogen adsorption and electron transfer processes. Palladium nanoparticles facilitate the dissociation of molecular hydrogen (H_2) into atomic hydrogen even at room temperature, significantly enhancing gas–material interactions.[53] This dissociative adsorption increases sensitivity and accelerates the response and recovery times. Additionally, the hydrogen spillover effect from Pd onto the COF expands the number of active sites, while the porous structure of the TAPT-COF supports efficient gas diffusion. The synergistic effect between Pd catalysis and COF porosity leads to an improved chemiresistive response, faster sensing kinetics, and high reversibility, making the Pd@TAPT-COF a highly promising material for room-temperature hydrogen sensing.[54]

2.3. Hydrogen sensing performance of the pristine TAPT-COF and Pd@TAPT-COF at different temperatures

To evaluate the influence of temperature on H_2 sensing behaviour, TAPT-COF and Pd@TAPT-COF sensors were tested at three different temperatures of 50 °C, 100 °C, and 150 °C at 1 ppm H_2 concentration. The corresponding response (R_a/R_g),

recovery times, and recovery percentages are summarized in Tables S7 and S8, and illustrated in Fig. 5e and f. The response (R_a/R_g) values of the TAPT-COF sensor at 50 °C, 100 °C and 150 °C were 2, 4, and 6 at 1 ppm, the response times were 4 s, 20 s, and 18 s, and the recovery times were 5 s, 13 s, and 15 s (Fig. 5e). Across all temperatures (50–150 °C), the sensor maintained a high average recovery efficiency of 99.6%, indicating stable and reversible sensing behaviour. Similarly, the Pd@TAPT-COF sensor exhibited superior performance compared to the pristine TAPT-COF at all temperatures. The response values were 3 at 50 °C, 5 at 100 °C, and 8 at 150 °C; the response times were 4 s, 13 s, and 17 s, and the recovery times were 6 s, 15 s, and 15 s (Fig. 5f). The highest recovery percentage of 99.8% was also recorded at 150 °C, reflecting excellent regeneration capability. This enhancement can be attributed to the catalytic activity of Pd NPs, which likely facilitates more efficient H_2 adsorption–desorption processes.

The chemiresistive sensing behaviour of the pristine TAPT-COF and Pd@TAPT-COF toward H_2 gas was further systematically evaluated. The dynamic response–recovery behaviour of the Pd@TAPT-COF at 1 ppm H_2 (Fig. 6a) reveals stable and repeatable resistance changes over multiple exposure cycles, indicating excellent reproducibility at 1 ppm H_2 and reversible interactions. The sharp decrease and recovery of resistance upon H_2 exposure suggest a rapid adsorption–desorption mechanism facilitated by the ''Pd'' sites. A comparative concentration-dependent (1–50 ppm) sensing study showed that the Pd@TAPT-COF exhibited a significantly enhanced response (R_a/R_g) toward H_2 compared to the pristine COF (Fig. 6b), which can be attributed to the catalytic role of Pd NPs in facilitating H_2 dissociation and charge carrier modulation. This was followed by selectivity studies (Fig. 6c and d) at a fixed concentration of 1 ppm for acetylene, xylene, toluene, ammonia, and hydrogen. The increase in sensing response with temperature can be understood from the temperature dependence of the Pd–H_2 interaction and H_2 spill-over kinetics. The comparable response at 25 °C and 50 °C suggests that Pd-assisted H_2 dissociation and the initial spill-over step have low activation energies, whereas at 150 °C, the activation barrier for H_2 dissociation and interaction is more effective, which promotes faster hydrogen spill-over and stronger charge-transfer interactions within the TAPT-COF, thereby producing a significantly higher response.[62] While the TAPT-COF showed moderate selectivity toward H_2, the Pd@TAPT-COF demonstrated remarkably enhanced selectivity, showing a significantly stronger response to H_2 compared to other interfering gases.

Although the Pd@TAPT-COF shows a higher sensing response at elevated temperatures (50–150 °C), the practical operating conditions for H_2 leak detection are room temperature because H_2 leakage typically occurs under uncontrolled ambient environments without an external heating source.[63] The higher response at elevated temperatures arises from faster Pd-catalysed H_2 dissociation and accelerated hydrogen spillover into the π-conjugated TAPT-COF, which enables charge transfer interactions. At 150 °C, thermal energy sufficiently overcomes the activation barriers for both dissociation and migration, accelerating hydrogen spill-over and enabling deeper penetration into the COF's conjugated framework. However, a continuous high-temperature operation can lead to more power consumption, baseline drift due to Pd → PdH_x cycling, reduced selectivity, and possible structural strain in the porous organic framework.[64]

The influence of relative humidity (RH) on sensor performance was assessed at 1 ppm H_2 under different RH levels (10–75%) (Fig. 6e and f). A gradual decrease in sensor response was observed with increasing RH for both COFs, which could be due to the viable adsorption of water molecules occupying the active sites.[65] Interestingly, the Pd@TAPT-COF showed a higher response under all humidity levels, suggesting improved moisture tolerance owing to stronger Pd–H_2 interactions.[66] Finally, long-term operational stability, a critical factor for practical sensing applications, was monitored for up to 15 days at 1 ppm (Fig. 6g and h). Both sensors exhibited minimal variations in their response values. This confirms the structural integrity and stability of the sensing interface under ambient conditions. Notably, the Pd@TAPT-COF maintained a consistently higher and more stable response over the entire duration, confirming its superior durability and reliability for long-term H_2 detection. These results collectively highlighted the Pd@TAPT-COF as a highly sensitive, selective, and stable sensor for low-concentration H_2 detection at room temperature for real-time environmental and industrial safety monitoring applications.

To evaluate the chemical, structural, and morphological integrity of the synthesised materials after hydrogen gas exposure, FTIR, PXRD, and SEM analyses were performed. The FTIR spectra of the TAPT-COF and Pd@TAPT-COF post-H_2 sensing revealed that the fundamental chemical framework remains largely unaffected. The prominent absorption band at 1622 cm^{-1} corresponds to the C═O stretching vibration of the keto group, confirming the presence of the β-ketoenamine linkage even after gas exposure. The peak around 1570–1580 cm^{-1} corresponds to the C═N stretching of the enamine group.[67] This suggests that the enamine group remains intact, suggesting the framework maintains its conjugated structure with observation of minor shifts or intensity reduction in the C═N and C–N stretching bands in the Pd@TAPT-COF (Fig. S10, SI). This could be due to weak interactions between Pd active sites and adsorbed hydrogen molecules (physisorption) without permanent disruption of the chemical structure. The powder X-ray diffraction patterns of both the TAPT-COF and Pd@TAPT-COF (Fig. S11, SI) after H2 sensing exhibited reflections consistent with the pristine samples. The dominant diffraction peak near ~4.7°, corresponding to the (100) plane, remains visible. This indicates the preservation of a 2D periodic layered structure. Additional peaks at ~8.1° (110) and ~13.1° (210), and higher-angle reflections confirmed the retention of long-range order. However, in the case of the Pd@TAPT-COF, a slight reduction in intensity and minor broadening of the (100) peak were observed after sensing, suggesting a modest decrease in crystallinity.[67,68] This can be attributed to framework flexibility and local rearrangement caused by interactions with hydrogen molecules at the Pd sites. The SEM analysis provides

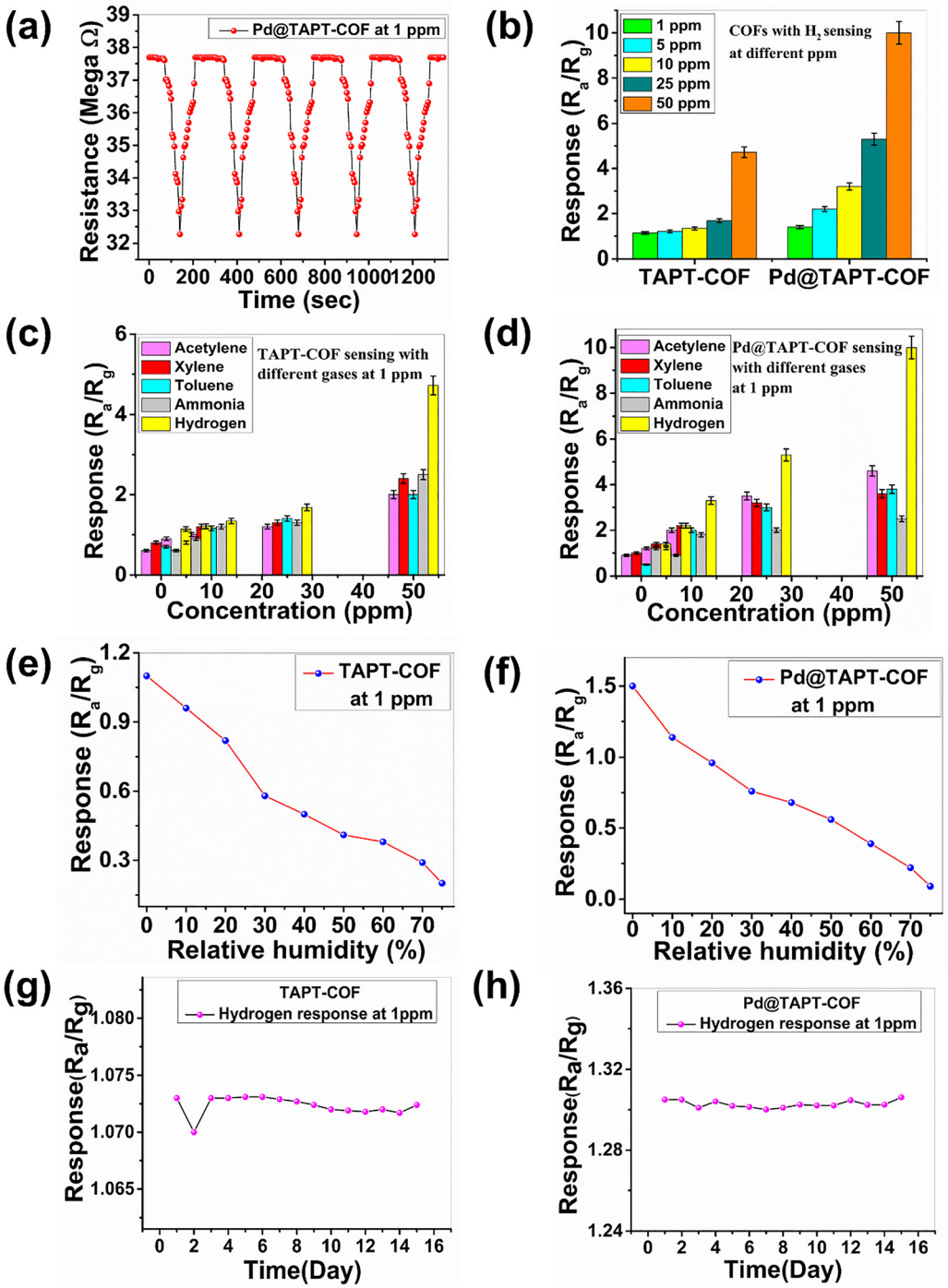

Fig. 6 (a) Reproducibility of the Pd@TAPT-COF sensor at 1 ppm, (b) sensing comparison of the TAPT-COF and Pd@TAPT-COF at different H_2 gas concentrations, (c) and (d) selectivity studies (acetylene, xylene, toluene, ammonia and hydrogen) of the TAPT-COF and Pd@TAPT-COF at different concentrations, (e) and (f) the response (R_a/R_g) of the TAPT-COF and Pd@TAPT-COF sensors to 1 ppm H_2 gas under varying relative humidity (RH) levels, and (g) and (h) long-term stability response of the TAPT-COF and Pd@TAPT-COF (up to 15 days).

insights into the morphological changes post-H_2 sensing. The TAPT-COF (Fig. S12a and b, SI) retains its characteristic flaky sheet-like morphology with a porous and interlinked network structure, and the Pd@TAPT-COF (Fig. S12c and d SI) also retains its layered sheet morphology. The sheets appeared slightly more compact and aggregated compared to the pristine TAPT-COF. The slight compaction of the layers is likely due to the weak hydrogen physisorption on Pd nanoparticles, leading to minor shrinkage or reorganization of the COF layers.[69] These post-sensing analyses collectively confirmed that both the TAPT-COF and Pd@TAPT-COF retained their structural and chemical integrity after hydrogen exposure, with the

Pd@TAPT-COF exhibiting slight framework reorganisation, supporting a reversible physisorption-driven sensing mechanism.[27,69]

2.4. Hydrogen sensing mechanism

The superior H_2 sensing performance of the Pd@TAPT-COF at ambient temperature can be attributed to a synergistic mechanism involving catalytic dissociation, charge transfer, and spillover effects.[25,70] Upon exposure to H_2 gas, molecular hydrogen diffuses through the porous COF matrix and interacts with the incorporated Pd NPs. Due to palladium's high affinity for hydrogen, H_2 undergoes dissociative chemisorption on the Pd surface to form adsorbed atomic hydrogen:

$$H_{2(g)} \rightarrow 2H_{(ads)} \quad (1)$$

$$Pd + xH_{(ads)} \rightleftharpoons PdH_x \quad (2)$$

These atomic hydrogens are subsequently adsorbed into the palladium matrix, forming palladium hydride (PdH_x) through a reversible adsorption process.[71] The formation of PdH_x reduces the work function of palladium, enabling electron transfer from PdH_x to the surrounding TAPT-COF in the Pd@TAPT-COF, leading to increased charge carrier density and improved conductivity.[71] Moreover, a portion of the dissociated hydrogen undergoes surface transfer from the Pd sites onto the TAPT-COF structure, a process known as hydrogen spillover. The atomic hydrogen interacts with electron-rich sites within the TAPT-COF, particularly keto groups and triazine nitrogen atoms, leading to localised polarization and further electronic perturbation. These interactions are efficiently transmitted through the extended π-electron system of the TAPT-COF (π-conjugated system), facilitating rapid charge delocalisation. While the strong interaction between Pd and H_2 allows low concentration detection under ambient conditions, the high surface area and porous structure of the Pd@TAPT-COF ensure rapid diffusion and accessibility to active sites. In comparison, the pristine TAPT-COF exhibited only weak physisorption interactions with H_2, resulting in minimal conductivity changes. Therefore, the superior sensing response of the Pd@TAPT-COF arises from the supportive effects of Pd-catalysed H_2 activation (eqn (1) and (2)), spillover-induced polarization, and the intrinsic charge transport properties of the COF[70]. It is also important to note the concentration-dependent sensing behaviour observed for the Pd@TAPT-COF. At low gas concentrations, the available Pd active sites are not fully occupied; therefore, the interactions between the Pd@TAPT-COF and different analyte gases are dominated by weak physisorption, resulting in similar response values across gases. However, at higher H_2 concentrations, Pd catalytically dissociates H_2 into atomic hydrogen, which subsequently undergoes spillover onto the COF. This spillover process leads to stronger charger transfer and a greater change in electrical conductivity compared to other gases, which do not undergo catalytic dissociation on Pd. Therefore, the Pd@TAPT-COF exhibits comparable responses to different gases at low concentrations, but exhibits markedly enhanced selectivity toward H_2 at higher concentrations (Fig. 7).

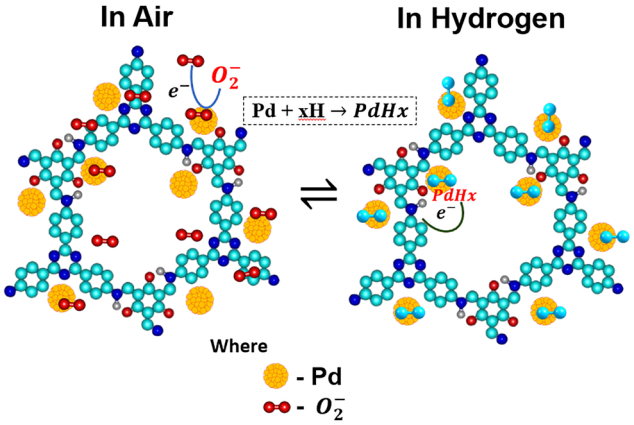

Fig. 7 Schematic representation of the hydrogen gas sensing mechanism.

Furthermore, comprehensive density functional theory (DFT) calculations were performed using the Gaussian 16 software package to support and understand the enhanced hydrogen sensing behaviour observed experimentally for the TAPT-COF and Pd@TAPT-COF.[72] Geometry optimisations and single-point energy calculations for the pristine COFs and their H_2-adsorbed counterparts were carried out using the B3LYP functional and the 6-311+G(d)* basis set[73,74] (Fig. S13a–d and Table S9, SI). GD3BJ was applied to improve the accuracy of non-covalent interaction modelling, particularly for the weakly bound H_2 molecule.[75,76] Three adsorption sites were studied: the keto-group site (site-1, C═O···H_2 region), the triazine-rich site (site-2, C–N···H_2 region), and, in the case of the Pd@TAPT-COF, the embedded Pd centre acts as site-3. These adsorption sites are illustrated in Fig. S14a, b and S15a, b (SI). The binding energies were calculated using eqn (1) (Section S4, SI) and are summarized in Tables S10 and S11 (SI). To assess the adsorption affinity and site selectivity, binding energy (E_{ads}) values were calculated at site-1 and site-2 for both the TAPT-COF and Pd@TAPT-COF. In the pristine TAPT-COF, the adsorption energies were found to be −57.77 kJ mol^{-1} (−0.599 eV) at site-1 and −69.96 kJ mol^{-1} (−0.725 eV) at site-2, suggesting weak physisorption primarily driven by van der Waals interactions. However, in the Pd@TAPT-COF, the binding energies at these sites increased dramatically to −484.57 kJ mol^{-1} (−5.022 eV) and −275.30 kJ mol^{-1} (−2.853 eV), indicating strong chemisorption. This enhancement is attributed to the catalytic activity of Pd, which facilitates dissociative adsorption of H_2 into surface-bound hydrogen atoms, forming PdH_x species and enabling charge redistribution across the framework. Although the binding energy at the Pd centre (site-3) was not directly computed, the substantial increase in E_{ads} at nearly COF sites suggests a synergistic effect, where Pd not only acts as a catalytic site but also enhances adsorption at adjacent functional groups. These results clearly demonstrated that the Pd@TAPT-COF presents three distinct hydrogen interaction sites, with the Pd centre serving as a catalyst that enhances adsorption energies and electronic response. This was further analysed using HOMO–LUMO energy levels, partial density of

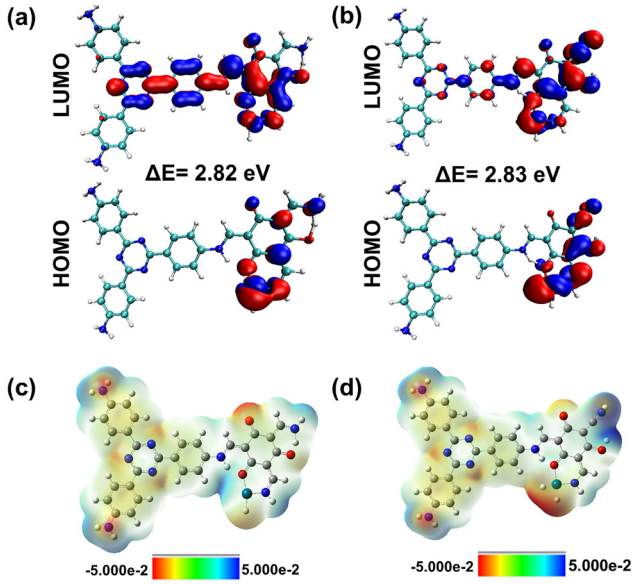

Fig. 8 HOMO and LUMO plots of the (a) Pd@TAPT-COF and (b) Pd@TAPT-COF-H_2. Electrostatic potential graphs of the (c) Pd@TAPT-COF and (d) Pd@TAPT-COF-H_2.

states (PDOS), natural bond orbital (NBO) analysis, and non-covalent interaction (NCI) mapping *via* reduced density gradient (RDG) plots. These theoretical studies offer molecular-level insight into the interaction of hydrogen with the framework and reveal how Pd incorporation modulates adsorption energetics and electronic structure.

To further understand the effect of Pd incorporation and H_2 interaction on the electronic structure of the TAPT-COF, HOMO–LUMO and electrostatic potential (ESP) analyses were performed. As shown in Fig. 8a and b, the HOMO and LUMO of the Pd@TAPT-COF and Pd@TAPT-COF-H_2 are predominantly localized over the π-conjugated framework and the Pd-interacting sites. The calculated energy gap (ΔE_g) for the Pd@TAPT-COF is found to be 2.82 eV, which is slightly increased to 2.83 eV upon H_2 adsorption. This slight variation in band gap is attributed to the formation of Pd–H species and the redistribution of electron density across the framework upon H_2 interaction.[77] Table S12 (SI) further confirmed this trend, where the pristine TAPT-COF showed a relatively larger band gap (3.56 eV), consistent with its lower conductivity and physisorptive nature. In contrast, the Pd@TAPT-COF exhibited a narrowed gap due to strong orbital interactions introduced by Pd doping. Notably, the Pd@TAPT-COF-H_2 systems at both site-1 and site-2 maintain similar gaps (~2.81–2.83 eV), highlighting their electronic stability under hydrogen exposure (Fig. S16a–d, SI). Electrostatic potential maps (Fig. 8c, d and Fig. S17a–d, SI) further revealed the distribution of electron-rich (red) and electron-deficient (blue) regions across the surface of the TAPT-COF and Pd@TAPT-COF in its H_2-adsorbed state. The ESP surface of the Pd@TAPT-COF showed localized negative potential around keto and nitrogen atoms, indicating favourable sites for hydrogen interaction. After H_2 adsorption, noticeable changes in the ESP intensity and distribution were observed, particularly near the active sites, suggesting polarization effects and localized charge redistribution induced by chemisorption.[78] Together, the HOMO–LUMO and ESP analyses proved that Pd incorporation decreases the energy gap and improves conductivity and H_2 electronic interactions.[79]

Building upon the HOMO–LUMO and ESP results, PDOS analysis further elucidated the electronic effects of H_2 adsorption on the TAPT-COF. As shown in Fig. 9a, the TAPT-COF-H_2 showed minimal changes near the Fermi level, consistent with the weak physisorption suggested by its low binding energy and limited orbital overlap. In contrast, Fig. 9b revealed that Pd@TAPT-COF-H_2 exhibits an increased density of states near the Fermi level, with noticeable contributions from Pd and H_2 orbitals.[80] This points to stronger orbital hybridization and enhanced electronic interaction at the Pd site. Comparable trends were observed at site-2 (Fig. S18a and b, SI), further supporting the catalytic and electronic role of Pd in enhancing H_2 adsorption. The NBO analysis was performed for the Pd@TAPT-COF to gain deeper insights into its electronic structure and charge transfer behaviour during H_2 adsorption. The corresponding data are provided in Table S13, SI (Pd@TAPT-COF), Table S14, SI (site-1, –C═O–H_2 region), and Table S15, SI

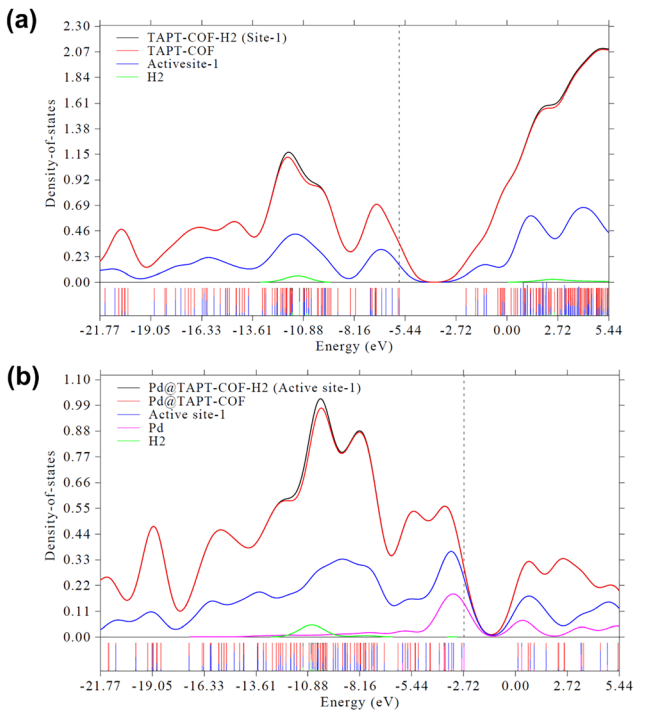

Fig. 9 (a) Projected density of states (PDOS) analysis of H_2 adsorption on the TAPT-COF. The PDOS of the TAPT-COF (black), TAPT-COF-H_2 (red), active site-1 (blue), and H_2 molecule (green) indicates a weak interaction between H_2 and the pristine COF. (b) Projected density of states (PDOS) analysis of H_2 adsorption on the Pd@TAPT-COF. The PDOS of the Pd@TAPT-COF (black), Pd@TAPT-COF-H_2 (red), active site-1 (blue), Pd (magenta), and H_2 molecule (green) indicates significant changes in electronic states upon H_2 adsorption.

(site-2, –C–N–H_2 region). The analysis revealed strong donor–acceptor interactions, particularly from the lone pair (LP) orbitals of oxygen atoms to the antibonding orbitals of the Pd center [LP(O) → LP*(Pd)],[81] with high second-order stabilization energies (E^2 values exceeding 150 kJ mol^{-1}), confirming significant charge delocalization toward Pd. Moreover, π(N–Pd) → π*(C–C) and π(C–N) → π*(C–C) interactions were observed across the conjugated framework, especially at both adsorption sites, which promote intramolecular charge redistribution. These interactions facilitate efficient electronic transfer between the Pd site and the TAPT-COF, enhancing the charge carrier density and electronic conductivity upon H_2 adsorption. These findings are consistent with the experimental sensing results and confirm that Pd plays a crucial role in facilitating charge transfer within the Pd@TAPT-COF during hydrogen sensing.

To further elucidate the nature of non-covalent interactions between hydrogen molecules and the COFs, reduced density gradient (RDG) analysis was performed[82,83] (Fig. 10). The RDG *vs.* sign(λ_2)ρ plots for the TAPT-COF and Pd@TAPT-COF, both before and after H_2 adsorption at two active sites (site-1: –C═O–H_2 and –C–N–H_2), provided key insights into the interaction strengths and types. In the pristine TAPT-COF (Fig. 10a), the RDG plot exhibited broad green regions near zero sign(λ_2)ρ values, indicating weak van der Waals interactions with minimal charge redistribution. The incorporation of Pd into the framework (Fig. 10b) results in an enhanced negative sign(λ_2)ρ region, which corresponds to the stronger attractive interactions between the framework and hydrogen molecules. This enhancement can be indicated by weak Pd–H coordination, occurring at the catalytically active Pd sites. For TAPT-COF-H_2 at site-1 and site-2 (Fig. 10c and e), the green spikes persist, but their intensities remain moderate, confirming physisorption dominated by non-specific interactions. In contrast, Pd@TAPT-COF-H_2 (Fig. 10d and f) showed significantly enhanced spikes in the negative region of sign(λ_2)ρ, reflecting stronger attractive

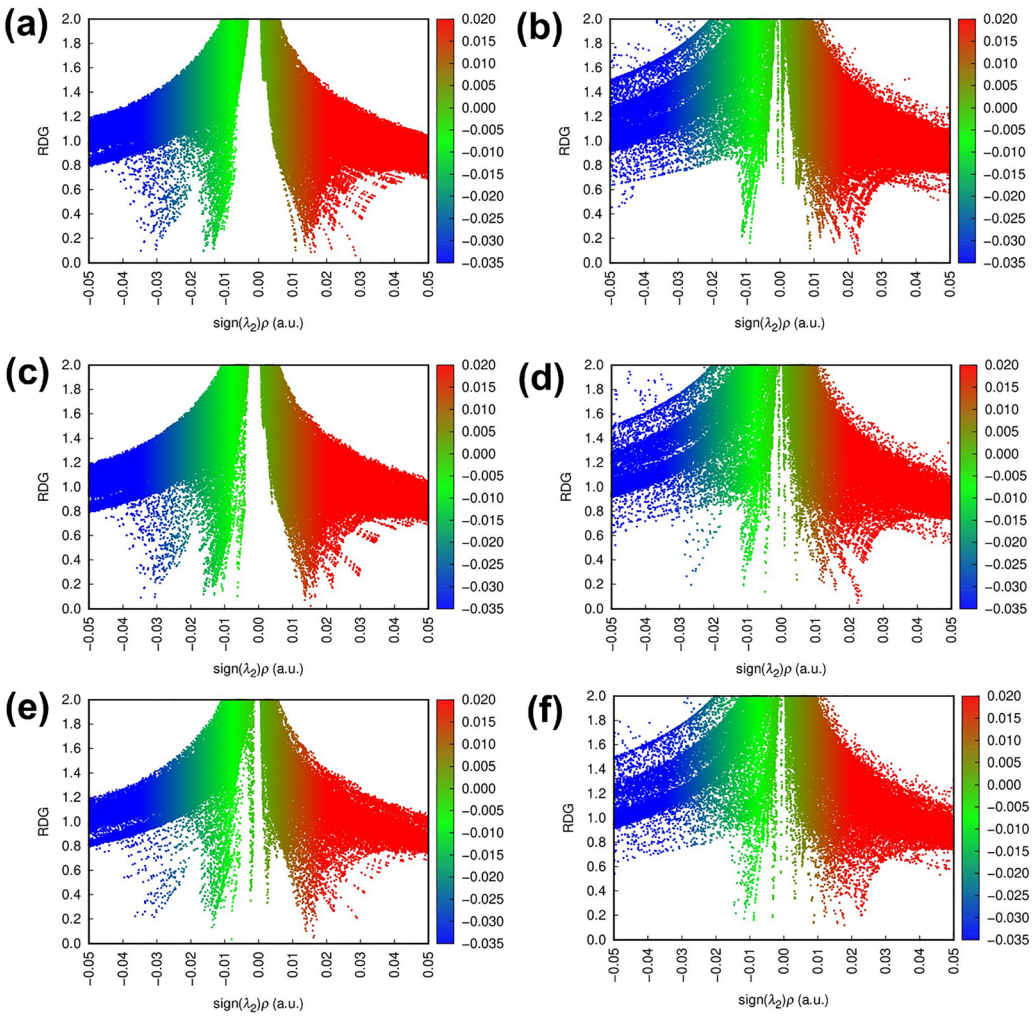

Fig. 10 Reduced density gradient (RDG) *vs.* sign(λ_2)ρ plots representing non-covalent interaction (NCI) analysis for the (a) TAPT-COF, (b) Pd@TAPT-COF, (c) TAPT-COF-H_2 at site-1, (d) Pd@TAPT-COF-H_2 at site-1, (e) TAPT-COF-H_2 at site-2, and (f) Pd@TAPT-COF-H_2 at site-2. The color scale indicates the strength and nature of interactions: blue (strong attractive interactions such as H-bonding), green (van der Waals interactions), and red (strong repulsion).

interactions, particularly near the Pd centre. These features correspond to chemisorption through partial electron transfer and hydrogen dissociation mechanisms. Overall, the RDG analysis confirmed that Pd doping enhances the strength and nature of non-covalent interactions in the TAPT-COF, supporting the observed increases in adsorption energy and improved sensing performance.

The DFT calculations revealed that Pd incorporation significantly enhances hydrogen sensing capability. The adsorption energies increase markedly in the Pd@TAPT-COF, indicating strong chemisorption compared to weak physisorption in the pristine TAPT-COF. A reduced HOMO–LUMO gap (−2.82 eV) intensified PDOS near the Fermi level and polarised ESP surfaces confirmed improved electronic interactions. NBO and RDG analyses further supported the enhanced charge transfer and stronger non-covalent interactions at Pd sites. These theoretical insights align well with experimental results, validating Pd's crucial role in boosting H_2 adsorption and sensing performance.

The enhanced sensing performance of the Pd@TAPT-COF over the pristine TAPT-COF arises from three synergistic effects introduced by Pd functionalisation: (i) palladium's intrinsic catalytic activity facilitates the dissociative chemisorption of H_2 molecules into atomic hydrogen, forming PdH_x species that lower the local electronic structure by lowering the work function and facilitating charge transfer to the TAPT-COF; (ii) the hydrogen spillover effect facilitates further interaction with nearby functional groups such as keto and triazine moieties, enhancing polarisation and conductivity; (iii) Pd incorporation of orbital hybridisation, as confirmed by PDOS and HOMO–LUMO analyses, improves electronic coupling and increases charge carrier density. These combined effects lead to faster response, higher sensitivity, and greater selectivity toward H_2 under ambient conditions, validating the Pd@TAPT-COF as an advanced material for practical hydrogen sensing applications.

3. Conclusion

In conclusion, this work highlights the Pd@TAPT-COF as a high-performance, room-temperature H_2 sensor through the rational integration of catalytically active Pd sites into a chemically robust β-ketoenamine COF. Post-synthetic functionalization introduced Pd nanoparticles that strongly coordinate to keto and imine moieties, as confirmed by solid-state ^{13}C NMR, FTIR, and XPS analyses. Nitrogen sorption analysis revealed that, despite a moderate reduction in surface area (from 200 to 150 $m^2\ g^{-1}$) and pore size (from 45.7 to 42.1 nm), the mesoporous network and slit porous structure were preserved, ensuring efficient gas diffusion. This structural optimization translated into outstanding sensing performance, with the Pd@TAPT-COF attaining a response (R_a/R_g) of 10, ultrafast response/recovery times (4 s/3 s at 1 ppm H_2), excellent selectivity against competing gases, and operational stability over repeated cycles. Post-sensing characterization revealed no structural degradation, supporting a reversible adsorption mechanism. The origin of the enhanced performance was further elucidated through DFT calculations, revealing a higher binding energy compared to the pristine COF (−5.022 eV), a reduced HOMO–LUMO gap (3.56 eV to 2.82 eV), and hybridized Pd–H states near the Fermi level. NBO, PDOS, and RDG analyses confirmed efficient Pd-framework charge transfer and non-covalent interactions from hydrogen spillover onto keto and triazine sites. This synergy of Pd catalysis, mesoporosity, and electronic tunability positions make the Pd@TAPT-COF a versatile, high-performance material for rapid, selective, and reusable hydrogen sensing, offering a strong potential sensor for deployment in energy safety and environmental monitoring applications.

Conflicts of interest

The authors declare no competing financial interests.

Data availability

The data that support the findings of this study are available in the supplementary information (SI) of this article. Supplementary information: details of the chemicals and reagents used for the synthesis of COF materials; characterization data such as optical spectroscopy studies; XPS analysis; surface analysis; electron microscopy studies; N_2-adsorption studies; UV-Vis DRS spectrum and thermal analysis graph; chemiresistive gas sensing fabrication and instrumental setup; characterization data of COF thin films after hydrogen sensing; theoretical studies of COFs and tables. See DOI: **https://doi.org/10.1039/d5qm00681c**.

Acknowledgements

Mr Sujith Benarzee acknowledges the financial support from the Department of Science and Technology (DST), Government of India, through the INSPIRE fellowship (INSPIRE code: IF210570) The authors thanks the CIF, GITAM Deemed to be University, for the facilities. The authors would also like to acknowledge the SAIF, DST-supported Institute NMR Facility at IISc Bangalore, for providing the solid-state NMR spectra.

References

1 T. Minezaki, P. Krüger, F. E. Annanouch, J. Casanova-Cháfer, A. Alagh, I. J. Villar-Garcia, V. Pérez-Dieste, E. Llobet and C. Bittencourt, Hydrogen sensing mechanism of WS_2 gas sensors analyzed with DFT and NAP-XPS, *Sensors*, 2023, **23**, 4623.
2 O. Nuzhdin, The Battle of Velikiye Luki in 1941 in the fates of the generals of the 22nd Ural Army, *Quaestio Rossica*, 2025, **13**(2), 409–417.
3 D. Guan, B. Wang, J. Zhang, R. Shi, K. Jiao and L. Li, *et al.*, Hydrogen society: from present to future, *Energy Environ. Sci.*, 2023, **16**, 4926–4943.

4 T. T. Le, P. Sharma, B. J. Bora, V. D. Tran, T. H. Truong, H. C. Le and P. Q. P. Nguyen, Fueling the future: a comprehensive review of hydrogen energy systems and their challenges, *Int. J. Hydrogen Energy*, 2024, **54**, 791–816.
5 S. J. M. Algayyim, K. Saleh, A. P. Wandel, I. M. R. Fattah, T. Yusaf and H. A. Alrazen, Influence of natural gas and hydrogen properties on internal combustion engine performance, combustion, and emissions: a review., *Fuel*, 2024, **362**, 130844.
6 M. Sand, R. B. Skeie, M. Sandstad, S. Krishnan and G. Myhre, *et al.*, Hydrogen leakage: an underestimated risk for the hydrogen economy, *Commun. Earth Environ.*, 2023, **4**, 185.
7 S. Evro, B. A. Oni and O. S. Tomomewo, Hydrogen production pathways: environmental and economic sustainability assessment, *J. Clean. Prod.*, 2024, **453**, 142635.
8 I. B. Ocko and S. P. Hamburg, Climate consequences of hydrogen emissions, *Atmos. Chem. Phys.*, 2022, **22**, 9349–9368.
9 Y. Luo, C. Zhang, B. Zheng, X. Geng and M. Debliquy, A review of hydrogen sensing based on semiconductor metal oxides, *Int. J. Hydrogen Energy*, 2017, **42**, 20386–20397.
10 X. Shao, D. Zhang, M. Tang, H. Zhang, Z. Wang, P. Jia and J. Zhai, Highly sensitive H_2 sensor based on Pd-loaded hierarchical porous SnO_2 microspheres, *Chem. Eng. J.*, 2024, 153676.
11 S. He, Y. Gui, Y. Wang and J. Yang, Highly sensitive Pd-decorated In_2O_3 nanotubes for hydrogen detection, *Nano Energy*, 2022, 108132.
12 C. Zhang, L. Yu, S. Li, L. Cao and X. He, *et al.*, Carbon nanosheets for high-performance gas sensing, *Carbon*, 2024, 119090.
13 Y. Gui, W. Zhang, S. Liu, Y. Li and J. Yang, *et al.*, Ultrasensitive hydrogen sensing via engineered semiconductor heterostructures, *Nano Energy*, 2024, 109498.
14 S. Zhang, D. Liu and G. Wang, Recent advances in hydrogen storage and sensing materials, *Molecules*, 2022, **27**, 2586.
15 W. Koo, H. Cho, D. Kim, Y. H. Kim, H. Shin, R. M. Penner and I. Kim, Chemiresistive Hydrogen Sensors: Fundamentals, Recent Advances, and Challenges, *ACS Nano*, 2020, **14**(11), 14284–14322.
16 M. E. DMello, R. C. Sahoo, R. Raghunathan, H. S. S. R. Matte, P. Yadav, G. V. Shanbhag and S. B. Kalidindi, Metal–organic framework-derived catalysts for hydrogen evolution reaction, *Int. J. Hydrogen Energy*, 2022, **47**, 9477–9483.
17 D. G. Wang, T. Qiu, W. Guo, Z. Liang and H. Tabassum, *et al.*, Hydrogen evolution electrocatalysis: fundamentals and materials design, *Energy Environ. Sci.*, 2021, **14**, 688–728.
18 D. A. Vazquez-Molina, G. S. Mohammad-Pour, C. Lee, M. W. Logan and X. Duan, *et al.*, Mechanically flexible and chemically stable covalent organic frameworks, *J. Am. Chem. Soc.*, 2016, **138**, 9767–9770.
19 S. Y. Ding, M. Dong, Y. W. Wang, Y. T. Chen, H. Z. Wang, C. Y. Su and W. Wang, Thioether-based fluorescent covalent organic frameworks, *J. Am. Chem. Soc.*, 2016, **138**, 3031–3037.
20 Z. Li, Y. Zhang, H. Xia, Y. Mu and X. Liu, Porous ionic covalent organic frameworks for selective ion sorption, *Chem. Commun.*, 2016, **52**, 6613–6616.
21 T. Hosokawa, M. Tsuji, K. Tsuchida, K. Iwase, T. Harada, S. Nakanishi and K. Kamiya, Electrocatalytic hydrogen evolution on cobalt porphyrin-based covalent organic frameworks, *J. Mater. Chem. A*, 2021, **9**, 11073–11080.
22 H. H. Hegazy, S. S. Sana, T. Ramachandran, Y. A. Kumar, D. K. Kulurumotlakatla, H. S. M. Abd-Rabboh and S. C. Kim, Recent advances in hydrogen storage materials for energy applications, *J. Energy Storage*, 2023, 109405.
23 D. Wang, D. Zhang and Q. Mi, Highly sensitive H_2 gas sensor based on Pd-functionalized ZnO nanorods, *Sens. Actuators, B*, 2021, 130830.
24 D. Zhang, D. Wang, W. Pan, M. Tang and H. Zhang, Enhanced hydrogen sensing performance using Pd-loaded SnO_2 nanostructures, *Sens. Actuators, B*, 2022, 131634.
25 X. Hu, J. Wang, S. Li, X. Hu, R. Ye, L. Zhou, P. Li and C. Chen, Engineering porous frameworks for enhanced gas adsorption and sensing, *RSC Adv.*, 2023, **13**, 14980–14990.
26 T. Chu, P. Tian, G. Wang, Y. Jia, S. Dai, C. Rong, B. Zhang and F. Z. Xuan, Atomically dispersed Pd sub-metallene on MXene enabling ultrafast hydrogen sensing at room temperature, *Adv. Mater.*, 2025, 2504603.
27 V. Krishnaveni, M. E. DMello, P. Sahoo, N. Thokala, V. R. Bakuru, K. Vankayala, K. Basavaiah and S. B. Kalidindi, Flexible COF–MOF hybrid films for enhanced hydrogen evolution reaction, *ACS Appl. Nano Mater.*, 2023, **6**, 10960–10966.
28 C. Kuru, C. Choi, A. Kargar, D. Choi, Y. J. Kim, C. H. Liu, S. Yavuz and S. Jin, High-performance hydrogen sensing using nanowire heterostructures, *Adv. Sci.*, 2015, 1500004.
29 X. Tang, P. A. Haddad, N. Mager, X. Geng, N. Reckinger, S. Hermans, M. Debliquy and J. P. Raskin, Graphene-based microhotplates for high-performance gas sensing, *Sci. Rep.*, 2019, **9**, 40257.
30 H. J. Zhu, M. Lu, Y. R. Wang, S. J. Yao, M. Zhang, Y. H. Kan, J. Liu, Y. Chen, S. L. Li and Y. Q. Lan, Ultrastable hydrogen evolution catalysts based on metal–organic frameworks, *Nat. Commun.*, 2020, **11**, 153.
31 J. Huang, X. Liu, W. Zhang, Z. Liu, H. Zhong, B. Shao, Q. Liang, Y. Liu and Q. He, Palladium-functionalized porous materials for hydrogen detection, *Chem. Eng. J.*, 2020, 127136.
32 R. Paul, A. Maibam, R. Chatterjee, W. Wang, T. Mukherjee, N. Das, M. Yellappa, T. Banerjee, A. Bhaumik, S. Venkata Mohan, R. Babarao and J. Mondal, COF-based photocatalysts for hydrogen evolution under visible light, *ACS Appl. Mater. Interfaces*, 2024, **16**, 22066–22078.
33 A. R. Abdellah, A. B. A. El-Adasy, A. A. Atalla, K. I. Aly and H. N. Abdelhamid, Covalent organic frameworks: design, synthesis, and applications in energy storage, *Microporous Mesoporous Mater.*, 2022, 111961.
34 M. Bashri, S. Kumar, P. Bhandari, S. Stephen, M. J. O'Connor, S. Gaber, T. Škorjanc, M. Finšgar, G. E. Luckachan, B. Belec, E. Alhseinat, P. S. Mukherjee and D. Shetty, Dynamic

covalent frameworks for efficient charge transport and catalysis, *ACS Appl. Mater. Interfaces*, 2025, **17**, 17804–17812.
35 S. Y. Ding, J. Gao, Q. Wang, Y. Zhang, W. G. Song, C. Y. Su and W. Wang, A two-dimensional covalent organic framework with high surface area and chemical stability, *J. Am. Chem. Soc.*, 2011, **133**, 19816–19822.
36 J. Liu, Y. Luo, Y. Song and F. Xu, Recent advances in COF-based adsorbents and sensors, *Microchem. J.*, 2024, 110341.
37 J. M. Seo, J. E. Lee, H. J. Noh, S. K. Kwak and J. B. Baek, Porous 2D materials for catalytic and sensing applications, *ACS Mater. Lett.*, 2022, **4**, 2282–2288.
38 C. Ayed, J. Yin, K. Landfester and K. A. I. Zhang, Photocatalytic hydrogen evolution using COF-based nanocomposites, *Angew. Chem., Int. Ed.*, 2023, 216159.
39 S. B. Nallamalla, N. K. Katari, A. J. M. Reddy, S. B. Jonnalagadda and S. B. Manabolu Surya, Zinc-encapsulating covalent organic frameworks for enhanced chemiresistive NH_3 sensing at room temperature, *RSC Adv.*, 2025, **15**(21), 16708–16723.
40 D. Zhu, M. Zhang, L. Pu, P. Gai and F. Li, Multifunctional COF architectures for electrochemical sensing, *Small*, 2021, 210499.
41 Ü. Yilmaz, H. Küçükbay, S. T. Çelikesir, M. Akkurt and O. Büyükgüngör, Synthesis of novel benzimidazole salts and microwave-assisted catalytic activity of in situ generated Pd nanoparticles from a catalyst system consisting of benzimidazol salt, $Pd(OAc)_2$ and base in a Suzuki–Miyaura reaction, *Turk. J. Chem.*, 2013, **37**, 721–733.
42 N. Thokala, K. Vankayala, K. Basavaiah and S. B. Kalidindi, *et al.*, Spontaneously decorated palladium nanoparticles on redox-active covalent organic framework for chemiresistive hydrogen gas sensing, *Int. J. Hydrogen Energy*, 2024, **81**, 270–279.
43 P. Pachfule, M. K. Panda, S. Kandambeth, S. M. Shivaprasad, D. D. Díaz and R. Banerjee, Multifunctional and robust covalent organic framework–nanoparticle hybrids, *J. Mater. Chem. A*, 2014, **2**, 7944–7952.
44 S. Bi, F. Meng, D. Wu and F. Zhang, Synthesis of vinylene-linked covalent organic frameworks by monomer self-catalyzed activation of Knoevenagel condensation, *J. Am. Chem. Soc.*, 2016, **144**, 3653–3659.
45 Y. Yang, H. Niu, W. Zhao, L. Xu, H. Zhang and Y. Cai, Ultrafine Pd nanoparticles loaded benzothiazole-linked covalent organic framework for efficient photocatalytic C–C cross-coupling reactions, *RSC Adv.*, 2020, **10**, 29402–29407.
46 Y. Li, K. Zuo, T. Gao, J. Wu, X. Su, C. Zeng, H. Xu, H. Hu, X. Zhang and Y. Gao, Bimetallic-docked covalent organic frameworks with high catalytic performance towards coupling/oxidation cascade reactions, *RSC Adv.*, 2022, **12**, 4874–4882.
47 C. Chen, Y. Liu, J. Zhou, X. He, C. Chen, G. Xiao, Y. Tang and W. Chen, A rapid response room-temperature hydrogen sensor based on a three-dimensional Pd–In_2O_3/rGO aerogel, *New J. Chem.*, 2024, **48**, 5866.
48 S. Yan, Y. Cao, Y. Su, B. Huang, C. Chen, X. Yu, A. Xu and T. Wu, Hydrogen sensors based on Pd-based materials: a review, *Sensors*, 2025, **25**, 3402, DOI: **10.3390/s25113402**.
49 X. Wu, Y. Zhang, M. Zhang, J. Liang, Y. Bao, X. Xia, K. Homewood, M. Lourenço and Y. Gao, An ultrasensitive room-temperature H_2 sensor based on a TiO_2 rutile–anatase homojunction, *Sensors*, 2024, **24**, 978.
50 Y.-W. Jang, J.-W. Jo, S. K. Park and J. Kim, Room-temperature gas sensors based on low-dimensional nanomaterials, *J. Mater. Chem. C*, 2024, **12**, 18609–18627.
51 P. Loomba, S. B. Nallamalla, S. Koppula, N. K. Katari and S. B. Manabolu Surya, Zinc-doped covalent organic frameworks as high-efficiency chemiresistors for acetylene gas detection, *RSC Adv.*, 2025, **15**, 26229–26239.
52 S. Y. Cho, H. Ahn, K. Park, J. Choi, H. Kang and H. T. Jung, Ultrasmall grained Pd nanopattern H_2 sensor, *ACS Sens.*, 2018, **3**, 1876–1883.
53 Y. H. Choi, D. H. Kim and S. H. Hong, $CuBi_2O_4$ prepared by the polymerized-complex method for gas-sensing applications, *ACS Appl. Mater. Interfaces*, 2018, **10**, 14901–14913, DOI: **10.1021/acsami.8b02439**.
54 I. Darmadi, F. A. A. Nugroho and C. Langhammer, High-performance nanostructured palladium-based hydrogen sensors - current limitations and strategies for their mitigation, *ACS Sens.*, 2020, **5**, 3306–3327.
55 N. Thokala, K. Vankayala, A. D. Gaonkar, G. Periyasamy, K. Fazl-Ur-Rahman, K. Valle, M. E. DMello, K. Basavaiah and S. B. Kalidindi, An exfoliated redox active imide covalent-organic framework for metal-free hydrogen gas sensing, *Sens. Diagn.*, 2023, **2**, 1176–1180.
56 W. T. Koo, Y. Kim, S. Kim, B. L. Suh, S. Savagatrup, J. Kim, S. J. Lee, T. M. Swager and I. D. Kim, Hydrogen sensors from composites of ultra-small bimetallic nanoparticles and porous ion-exchange polymers, *Chem*, 2020, **6**, 2746–2758.
57 W.-B. Jung, S.-Y. Cho, B. L. Suh, H.-W. Yoo, H.-J. Jeon, J. Kim and H.-T. Jung, Polyelemental nanolithography via plasma ion bombardment: from fabrication to superior H_2 sensing application, *Adv. Mater.*, 2019, **31**, 1805343.
58 C. Kuru, D. Choi, A. Kargar, C. Choi, Y. J. Kim, C. H. Liu, S. Yavuz and S. Jin, High-performance flexible hydrogen sensor made of WS_2 nanosheet–Pd nanoparticle composite film, *Nanotechnology*, 2016, **27**, 195501, DOI: **10.1088/0957-4484/27/19/195501**.
59 A. Ibrahim, U. B. Memon, S. P. Duttagupta, I. Mahesh, R. K. S. Raman, A. Sarkar, G. Pendharkar and S. S. V. Tatiparti, Nanostructured palladium-impregnated graphitic carbon nitride composite for efficient hydrogen gas sensing, *Int. J. Hydrogen Energy*, 2020, **45**, 10623–10636.
60 W. Wu, Z. Liu, L. A. Jauregui, Q. Yu, R. Pillai, H. Cao, J. Bao, Y. P. Chen and S.-S. Pei, Wafer-scale synthesis of graphene by chemical vapor deposition and its application in hydrogen sensing, *Sens. Actuators, B*, 2010, **150**, 296–300.
61 Y. Pak, S. M. Kim, H. Jeong, C. G. Kang, J. S. Park, H. Song, R. Lee, N. Myoung, B. H. Lee, S. Seo, J. T. Kim and G. Y. Jung, Ultrasensitive and flexible hydrogen sensor based on Pd-decorated graphene, *ACS Appl. Mater. Interfaces*, 2014, **6**, 13293–13298.
62 T. Hübert, L. Boon-Brett, G. Black and U. Banach, Hydrogen sensors – A review, *Sens. Actuators, B*, 2011, **157**, 329–352.

63 S. Yan, Y. Cao, Y. Su, B. Huang, C. Chen, X. Yu, A. Xu and T. Wu, Hydrogen sensors based on Pd-based materials: a review, *Sensors*, 2025, **25**, 3402.
64 M. Choudhary, S. Singh, A. K. Sinha, S. Krishnamurthy, K. Saravanan, A. Chawla, D. K. Avasthi, S. Manna, V. Chawla and S. Wadhwa, Highly sensitive hydrogen gas sensor based on Pd-loaded ZnO nanostructures, *Chem. Eng. J.*, 2024, 157604.
65 T. Wen, X. Ma, Y. Huo, R. Guo, S. Zhang, Y. Han, Y. Liu, Y. Ai and X. Wang, Adsorption and sensing behavior of hydrogen on engineered porous materials, *Environ. Sci. Adv.*, 2023, **3**, 177–185.
66 Y. Zhang, W. Zhang, Q. Li, C. Chen and Z. Zhang, Room-temperature hydrogen sensing using Pd-decorated SnO_2 nanoarrays, *Sens. Actuators, B*, 2020, 128733.
67 Y. Li, M. Liu, J. Wu, J. Li, X. Yu and Q. Zhang, Recent advances in optical hydrogen sensors, *Front. Optoelectron.*, 2022, **15**, 228–246.
68 J. Li and B. Chen, Adsorptive separation in covalent organic frameworks (COFs): from fundamentals to applications, *Chem. Sci.*, 2024, **15**, 9874–9892.
69 Q. Liu, W. Xu, H. Huang, H. Shou, J. Low, Y. Dai, W. Gong, Y. Li, D. Duan, W. Zhang, Y. Jiang, G. Zhang, D. Cao, K. Wei, R. Long, S. Chen, L. Song and Y. Xiong, Boosting hydrogen evolution by engineering active sites in 2D materials, *Nat. Commun.*, 2024, 46923.
70 Y. T. Li, W. G. Cui, Y. F. Huo, L. Zhou, X. Wang, F. Gao, Q. Zhang, W. Li and T. L. Hu, Ultra-stable porous frameworks for hydrogen-energy applications, *Mater. Horiz.*, 2025, **12**, 2351–2359.
71 Q. Li, L. Wang, A. Xiao, L. Zhu and Z. Yang, Advances in hydrogen storage materials based on porous frameworks, *Int. J. Hydrogen Energy*, 2025, **136**, 1282–1305.
72 M. J. Frisch, G. W. Trucks, H. B. Schlegel, *et al. Gaussian 16, Revision C.01*, Gaussian Inc., Wallingford CT, 2016.
73 E. Torres and G. A. DiLabio, Improved hydrogen-bonding energetics from dispersion-corrected density functional theory, *J. Phys. Chem. Lett.*, 2012, **3**, 1738–1744.
74 C. Lee, W. Yang and R. G. Parr, Development of the Colle–Salvetti correlation-energy formula into a functional of the electron density, *Phys. Rev. B:Condens. Matter Mater. Phys.*, 1988, **37**, 785–789.
75 S. Grimme, S. Ehrlich and L. Goerigk, Effect of the damping function in dispersion-corrected density functional theory, *J. Comput. Chem.*, 2011, **32**, 1456–1465.
76 N. Sinha and S. Pakhira, Adsorption and sensing properties of gas molecules on 2D materials: a DFT study, *Mol. Syst. Des. Eng.*, 2022, **7**, 577–591.
77 A. Soltani, M. B. Javan, M. S. Hoseininezhad-Namin, N. Tajabor, E. T. Lemeski and F. Pourarian, Electronic and optical properties of MXene-based nanostructures: a DFT investigation, *Synth. Met.*, 2017, **234**, 1–8.
78 E. A. Bittner, K. Merkel and F. Ortmann, Charge transport in 2D materials: a computational perspective, *npj 2D Mater. Appl.*, 2024, 00496.
79 H. Joshi and S. Pakhira, Gas adsorption and electronic response of modified graphene sheets: a computational analysis, *ChemPhysChem*, 2024, 000237.
80 Y. Yan, Y. Zhao, X. Chen, Z. Lu, Y. Peng, Z. Chen and Q. Xu, Design strategies for efficient hydrogen evolution catalysts in MOFs and COFs, *Chem. Eur. J.*, 2024, 01122.
81 M. Yoosefian and N. Etminan, Hydrogen adsorption on doped graphene: a DFT investigation, *Physica E*, 2016, **81**, 116–121.
82 R. Bermeo-Campos, L. G. Arellano, Á. Miranda, F. Salazar, A. Trejo-Baños, R. Oviedo-Roa and M. Cruz-Irisson, Hydrogen storage and sensing properties of porous nanostructured composites, *J. Energy Storage*, 2023, 109205.
83 H. O. Taha, F. El-Shemy and M. M. Hassan, Structural and electronic properties of hydrogen-rich solids: implications for hydrogen storage, *Egypt. J. Solids*, 2024, **46**, 134–177.